



Article

Bimodal Porosity and Stability of a TiO₂ Gig-Lox Sponge Infiltrated with Methyl-Ammonium Lead Iodide Perovskite

Salvatore Sanzaro ^{1,2}, Federico Zontone ³, David Grosso ⁴, Thomas Bottein ⁴, Fortunato Neri ² , Emanuele Smecca ¹, Giovanni Mannino ¹, Corrado Bongiorno ¹, Corrado Spinella ¹, Antonino La Magna ¹ and Alessandra Alberti ^{1,*}

¹ National Research Council-Institute for Microelectronics and Microsystems (CNR-IMM), Zona Industriale-Strada VIII n°5, 95121 Catania, Italy; salvatore.sanzaro@imm.cnr.it or ssanzaro@unime.it (S.S.); emanuele.smecca@imm.cnr.it (E.S.); giovanni.mannino@imm.cnr.it (G.M.); corrado.bongiorno@imm.cnr.it (C.B.); corrado.spinella@imm.cnr.it (C.S.); antonino.lamagna@imm.cnr.it (A.L.M.)

² Department of Mathematical and Computational Sciences, Physics and Earth Sciences, University of Messina, Viale F. Stagno d'Alcontres 31, 98166 Messina, Italy; fneri@unime.it

³ ESRF, The European Synchrotron, CS40220, 38043 Grenoble CEDEX 9, France; zontone@esrf.fr

⁴ Institut Matériaux Microélectronique Nanosciences de Provence (IM2NP) Aix-Marseille Université, 13397 Marseille CEDEX 20, France; david.grosso@univ-amu.fr (D.G.); thomas.bottein@im2np.fr (T.B.)

* Correspondence: alessandra.alberti@imm.cnr.it

Received: 2 August 2019; Accepted: 6 September 2019; Published: 11 September 2019



Abstract: We created a blend between a TiO₂ sponge with bimodal porosity and a Methyl-Ammonium Lead Iodide (MAPbI₃) perovskite. The interpenetration of the two materials is effective thanks to the peculiar sponge structure. During the early stages of the growth of the TiO₂ sponge, the formation of 5–10 nm-large TiO₂ auto-seeds is observed which set the micro-porosity (<5 nm) of the layer, maintained during further growth. In a second stage, the auto-seeds aggregate into hundreds-of-nm-large meso-structures by their mutual shadowing of the grazing Ti flux for local oxidation. This process generates meso-pores (10–100 nm) treading across the growing layer, as accessed by tomographic synchrotron radiation coherent X-ray imaging and environmental ellipsometric porosimetry. The distributions of pore size are extracted before (>47% V) and after MAPbI₃ loading, and after blend ageing, unfolding a starting pore filling above 80% in volume. The degradation of the perovskite in the blend follows a standard path towards PbI₂ accompanied by the concomitant release of volatile species, with an activation energy of 0.87 eV under humid air. The use of dry nitrogen as environmental condition has a positive impact in increasing this energy by ~0.1 eV that extends the half-life of the material to 7 months under continuous operation at 60 °C.

Keywords: Ti-oxides; perovskites; blend; nano-scale; sputtering; Thornton; shadowing

1. Introduction

Titanium dioxide (TiO₂), since the discovery of its application to water photolysis by Fujishima and Honda in 1972 [1], has progressively raised interest in many different fields such as for photocatalytic degradation of pollutants [2–4], photocatalytic CO₂ reduction into energy fuels [5–8], water splitting [9–11], solar cells and photonics [12,13], sensors [14–16], supercapacitors [17,18], biomedical devices [19–21] and lithium-ion batteries [22–24].

In the photovoltaic field, recent advances were linked to the application of porous TiO₂ in hybrid solar cell architecture with efficiency that consequently went up strikingly rapidly [25] thanks to the new

ideas of M. Grätzel (dye solar cells, DSC) [26,27] and T. Miyasaka (perovskite solar cells, PSC) [28–30]. DSCs, with their structure and operation mechanism [31–38], represent the precursor technology of PSCs that, in their original architecture, have a mesoporous TiO₂ layer as scaffold to exchange the photo-generated carriers. Collection and injection efficiencies, comprising the parasitic diode operation, are indeed related to the structural properties of this scaffold. Additionally, since perovskite are required to form an interconnected blend with its scaffold, issues related to the accessibility of the TiO₂ pores, effectiveness of the perovskite reaction [39,40], and the stability and durability of the blend [41–53] need to be faced. In this respect, the pore filling capability is a parameter of high technological impact [54].

The most diffused and versatile way to grow a mesoporous TiO₂ scaffolds is by chemical methods. They can generate a large plethora of fascinating hierarchical and mesoporous structures [55–57] with high infiltration capability.

Standard physical growth methods are, instead, less performing in creating porous structures, and they are mostly based on the semi-empirical Thornton's approach [58,59]. As a step forward, cauliflower [60], penniform [61] or zig-zag [62] structures can be found in the literature. Some other attempts to increase the TiO₂ layer porosity were done using Ti nano-structures [14,63–70] deposited by sputtering in glancing angle configuration (GLAD) [71] and subsequently oxidized by ex-situ processes. Other approaches in the literature are based on the use of an array of template materials (e.g., polystyrene nano-spheres) to exploit their shadowing effect during TiO₂ growth [72]. All the existing approaches add complexity to the fabrication process (need of external oxidation or templating layers or seeds), in a countertrend with the request of high production throughput.

In our previous work [48], we initiated a method called gig-lox (grazing incidence geometry with local oxidation) to grow multi-porosity oxide layers by modified sputtering processes and demonstrated that gig-lox-based PSCs exhibit comparable efficiency with respect to devices made with standard chemically synthesized TiO₂ nano-structures, even if scaling down the thickness of the scaffolding layer. In addition, the electrical behavior of functionalized TiO₂ gig-lox layers unveiled [49] its high injection capability and high collection efficiency of photo-generated carriers. The method used is up-scalable, reliable and indeed industrially implementable, solvent-free, and can be, in principle, extended to any reactive metallic source to produce porous oxides. The multi-scale-porosity (micro and meso) represents a key parameter to allow material of different size (and nature) intimately entering into the TiO₂ scaffold and forming an active interacting (chemically and physically). In this respect, disclosing the early stage of formation of the gig-lox bimodal porosity and its capability to establish stable blends with photo-active perovskites would open the field for its industrialization in view of high throughput and indeed of low-cost production of solar devices.

In this framework, the paper illustrates the structural properties of the gig-lox TiO₂ sponge since the early stage of the material growth. We illustrate the mechanism of growth by auto-seeds and we disclose the bimodal pore structure (micro- and meso-pores [73,74]) using advanced technique such as tomographic coherent synchrotron X-ray-based diffraction imaging (CXDI) and environmental ellipsometric porosimetry (EEP). The capability of the gig-lox structure to host hybrid perovskite materials (i.e., CH₃NH₃PbI₃, hereafter called MAPbI₃, being the most explored for light harvesting) is here exploited and investigated. The gig-lox process is conceived to be compatible with any kind of substrate and is up-scalable for high production throughput. We demonstrate that our gig-lox TiO₂ scaffold blended with MAPbI₃ has a high stability and durability, and that the degradation process is mostly related to the eventual presence of an adverse environment rather than to the multiple interfaces established inside the blend. The mainstays of the growth procedure could be extended to other oxides of technological interest.

2. Materials and Methods

2.1. TiO₂ Gig-Lox Deposition

TiO₂ gig-lox layer is deposited in a customized DC-pulsed (Direct Current) sputtering equipment (Kenosistec S.r.l., Milano, Italy) we exploited the grazing incidence geometry of the titanium source assisted by the local oxidation (gig-lox) of the Ti species landing on the substrate to grow porous TiO₂ layers with multiple size porosity [73,74]. The deposition method and its mainstays are fully described in our previous papers [37,48,49].

2.2. Perovskite Preparation

Perovskite materials were deposited by solution processing on TiO₂ gig-lox layer, deposited by DC-pulsed sputtering on corning glass substrates. After TiO₂ deposition, a thermal annealing at 500 °C for 5 min in simulated dry air (80% N₂ and 20% O₂) was performed on the sample to assure anatase phase formation. Before perovskite deposition, the sample was treated by UV-O₃ for 10 min to clean the surface and avoid the presence of contaminants. Deposition of the perovskite films was performed in a dry room with a monitored humidity (~20%) by a CI-assisted one step deposition. A 40 wt% solution of PbCl₂ and methyl-ammonium iodide (MAI) (ratio 1:3) in dimethyl-formamide (DMF) was prepared at 70 °C under stirring for 1 h (Sigma Aldrich Co., St. Louis, MO, USA). The solution was spin coated on TiO₂ at 1200 rpm for 30 s; after that the rotational speed was increased to 2000 rpm for 6 s and subsequently to 4500 rpm for 24 s. During spin coating, 1 mL of toluene was dripped onto the substrate as solvent treatment to form a homogenous film. The substrates were then placed on a hot plate which was raised up to 90 °C for 40 min, up to 100 °C for 10 min and finally to 110 °C for 10 min to complete the evaporation of the solvent [42]. The as-deposited MAPbI₃ layers have comparable average thickness (~350 nm). The sample was stored in vials under a dry nitrogen atmosphere immediately after preparation to avoid triggering any degradation before the analyses.

2.3. X-ray Reflectivity and X-ray Diffraction Method

X-ray reflectivity (XRR) and X-ray diffraction (XRD) measurements were done using a D8-Discover Bruker AXS diffractometer equipped with a Cu-K_α source/Goebel mirror (Bruker Corporation, Billerica, MA, USA) and eventually soller slits at the primary beam, and with variable slits and detector at the secondary path.

2.4. Transmission Electron Microscopy Method

Transmission electron microscopy (TEM) analyses were done in plane-view and cross-section using a JEOL JEM 2010 microscope operating at 200 kV (JEOL Ltd., Akishima, Tokyo, Japan).

2.5. Scanning Transmission Electron Microscopy Method

Scanning transmission electron microscopy (STEM) images were acquired at 200 kV in scanning mode using a high angle annular dark field detector in Z-contrast configuration using a Jeol ARM200 equipped with a cold FEG electron source, CEOS condenser aberration corrector and at 100 mm² (JEOL Ltd., Akishima, Tokyo, Japan).

2.6. CXDI Method

CXDI analysis was performed using the equipment located at the beamline ID10 at the European Synchrotron Radiation Facilities in Grenoble, France (ESRF, Grenoble, France). The strength of the CXDI technique resides in the ability of high-resolution imaging, in principle limited by the highest q-vector where speckles are measurable. CXDI relies on a numerical algorithm that allows to phase the Fourier space to the real space when speckles are over-sampled [75–77]. CXDI is a powerful tool for providing a 3D image of the outer and the inner structures of micro-particles with a resolution of a few

tens of nanometers [75,78] thus giving access to the full description of the morphology of the particles like porosity and specific surface area.

Fragments of TiO₂ scaffolds were dispersed on the surface on a Si₃N₄ membrane via a gentle mechanical scratching of the support. Isolated micrometric particles were selected using an on-axis optical microscope. The measurements were performed using 8.1 keV radiation produced by the undulator source of the ID10, monochromatized by a Si(111) pseudo channel-cut monochromator and focused by compound refractive lenses at the sample location. The final beam was defined by a 10 μm square-shaped aperture of rollerblade slits and had an average intensity of 6×10^{10} ph/s. Tomographic series of 2D coherent small-angle speckle patterns were recorded by a Maxipix detector with 516 × 516 pixels located 3.280 m downstream the sample, resulting in a voxel size of 17.8 nm in the real space reconstructions and a maximum field-of-view of ~3 μm (linear oversampling ~3). The tomographic scans around the normal to the membrane surface were spanning an angular range of 162° for the particles of TiO₂ and TiO₂ with PbI₂, 144° for the particle with MAPbI₃, all of them with 0.25° angular step. A beam-stop prevented the direct beam to damage the detector with only a partial obstruction of the central speckles thanks to a careful alignment. The 2D projections were assembled to build the 3D Fourier space with 512 × 512 × 512 resolution elements that was phased by a combination of hybrid input–output and error-reduction algorithms [78]. Finally, 20 reconstructions were averaged to account for high frequency variations in the convergence due to noise. The conversion into absolute units was performed according to the beamline parameters (incidence intensity and beam size) and exposure time of the single frames (27 s for the TiO₂ particle, 15 s for the other two, TiO₂ with MAPbI₃ and TiO₂ with PbI₂).

2.7. Spectroscopic Ellipsometry Method

Spectroscopic ellipsometry (SE) data were collected using a J.A. Woollam VASE instrument (J.A. Woollam Co., Lincoln, NE, USA). Measurements were performed in a vertical configuration, which is better suited for transparent samples in order to measure on the same point ellipsometric and transmittance data. Optical spectra were recorded from 300 to 2100 nm (step 5 nm) at 55°, 60° and 65°. An initial model of the optical transitions was built for each layer constituting the sample. The TiO₂ layer was modelled by using a single Tauc-Lorentz oscillator and the surface roughness by the Bruggeman effective medium approximation (EMA). The technique was mainly used to measure the average porosity of the layer.

2.8. EEP Method

EEP was investigated using a visible (from 370 to 1000 nm) variable angle spectroscopic ellipsometer (ESM 300 Woollam) with an atmospheric control chamber [79] (J.A. Woollam Co., Lincoln, NE, USA). Isopropanol (Sigma Aldrich Co., St. Louis, MO, USA) was selected as the adsorbate and was fluxed into the chamber over the film. The volume of adsorbed and capillary condensed isopropanol was followed through time-resolved measurement of the refractive index variation upon the relative pressure of the adsorbate (P/P_0). The volume of adsorbate was deduced from the evolution of the refractive index using the Cauchy models and the Bruggeman Effective Medium Approximation (J.A. Woollam CompleteEASE software). The pore size distribution was then plotted using Kelvin's equation and by using a model of cylindrical pores.

3. Results and Discussion

3.1. Auto-Seeds Formation: XRR and TEM Analyses

We started by investigating the early stages of the material growth to disentangle the assembly process. We stopped the growth at the first 12 nm, 23 nm and 39 nm of material, as measured by SE and XRR. The XRR curves acquired on those samples are shown in Figure 1a in comparison with the simulated profile of an ideal flat compact TiO₂ layer supposed to have anatase density [15]. In the

figure, it is worthy to note that the critical angle for total external reflection, linked to the square root of the electronic surface density of the material, in the thinnest layer is largely under the reference (simulated profile in Figure 1a) while it progressively increases during further growth without ever matching the ideal value. This finding implies that the electronic density of the material is less than what is exposed in a compact amorphous TiO_2 phase, conversely providing indication that a porous layer has been grown. According to this, the experimental XRR curves can be shaped using electronic density and roughness as main fitting parameters. The average porosity values, in agreement with the SE findings, are shown in Figure 1b using the equation:

$$P(\%V) = \left[1 - \left(\frac{\rho_{\text{sample}}}{\rho_{\text{bulk}}} \right) \right] \times 100, \quad (1)$$

where in ρ_{sample} is the measured density and ρ_{bulk} is the density of the compact TiO_2 reference.

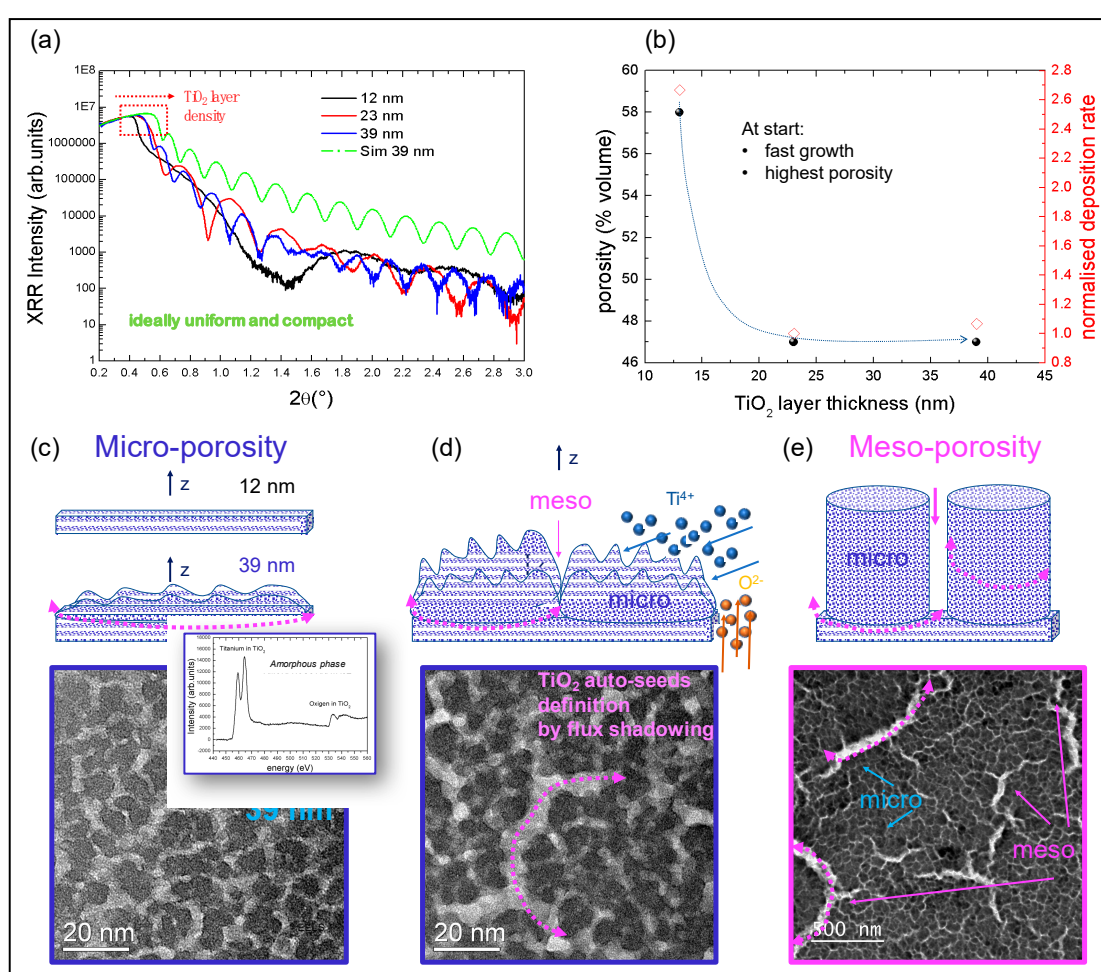


Figure 1. (a) X-ray reflectivity (XRR) profile of starting layers of different thickness, compared to the ideal case of a compact flat amorphous TiO_2 layer in the anatase polymorph. (b) porosity and deposition rate as a function of the grown thickness. Plane-view transmission electron microscopy (TEM) analyses of (c) a layer containing auto-seeds (39 nm); (d) a thicker layer with meso-pores starting to be defined; (e) a final layer (400 nm) with meso- and micro-porosity defined on a large scale (cross-section in Figure 2). The schematic provides the overall scenario during the initial growth, starting from the first minutes (transient) wherein a matrix of small TiO_2 grains and micro-pores are equally distributed and originated in a Thornton-like regime (high Ar pressure). During further growth, a network of larger TiO_2 auto-seeds gives rise to grazing incidence geometry with local oxidation (gig-lox) columns separated by meso-pores due to shadowing under rotation (steady state growth).

In the same graph, the deposition rate, normalized to the final plateau value (4 nm/min), was superimposed using red symbols. The cross-correlation of the data provides the scenario of a TiO₂ growth occurring through: (1) a first (transient) regime wherein the deposition rate is high and this corresponds to the maximum porosity value; (2) a second regime in which porosity and deposition rate approach steady-state values of ~47% volume and ~4 nm/min, respectively. The presence of a first layer with high porosity (~12 nm-thick) was included for fitting the profiles of thicker layers. Above this porous basement, nanometric auto-seeds (10–20 nm in diameter, separated by gaps, namely micro-pores, initially of 2–10 nm in size) are statistically generated introducing a surface roughening in the layer (Figure 1c). Their growth, according to the gig-lox method [37], is assisted by a progressive bottom-up local oxidation (lox) via an independent oxygen flux impinging onto the growing front [48,49]. The sample is under rotation during growth to assure a uniformity in thickness with a proper internal nano-structuration. The establishment of tens-of-nm-large TiO₂ auto-seeds on the sample surface is demonstrated by TEM analyses in plane-view, as that shown in Figure 1c done on the 39 nm-thick layer. In the inset, the electron energy loss spectroscopy (EELS) spectrum testifies a Ti:O = 1:2 stoichiometry and a mostly amorphous arrangement of the building-block. A macro-assembly process occurs during further growth by the progressive statistical drawing of meso-borders (meso-pores) by a shadowing action that selects the sites for ad-atoms attaching and finally brings together adjacent nano-seeds into larger meso-columns (Figure 1d,e). The resulting material is a TiO₂ sponge with a double-scale porosity. Shadowing and local oxidation are the mainstays of the process that can be applied to any substrate and oxide for thickness up-scalable to (at least) 1000 nm. The final structure of TiO₂ layers grown under steady-state conditions was described in refs [15,48,49] by TEM and SEM analyses and exploited for application in different fields. In what follows, insights on the double-scale porosity (meso and micro) will be gained by CXDI, a new methodology for imaging and tomography based on coherent synchrotron radiation, and by ellipsometric nano-porosimetry to explore to what extent the sponge can interconnect a perovskite material.

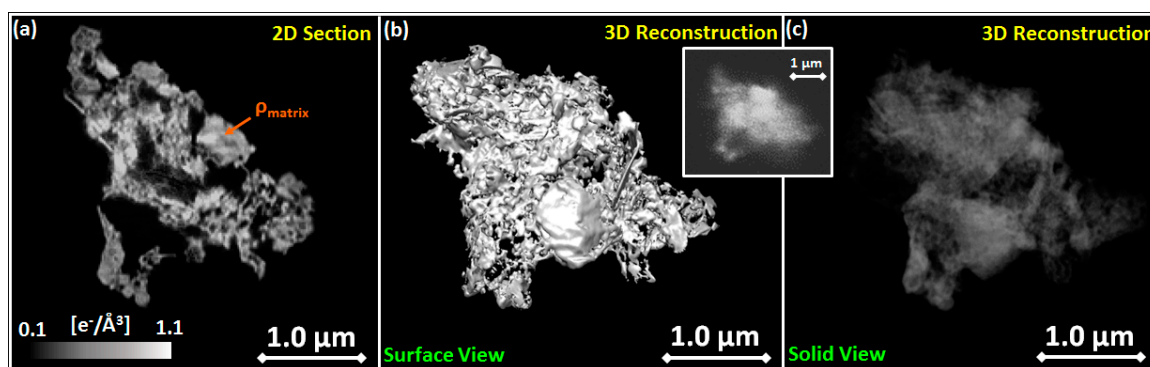


Figure 2. Coherent X-ray diffraction imaging (CXDI) reconstruction of a TiO₂ gig-lox portion representing: (a) central section showing the density ρ_{matrix} being smaller than anatase; (b) 3D reconstruction showing the morphology of the sample at its surface (surface view) and (c) 3D reconstruction based on the integrated electron density (see also Figure 5). Inset: Environmental Scanning Electron Microscopy (ESEM) image used as benchmark of the CXDI reconstruction.

3.2. Bimodal Porosity Investigation

3.2.1. CXDI Analyses

We imaged the 3D architecture of a TiO₂ gig-lox layer 400 nm-thick, grown at the steady state, using non-conventional tomographic coherent X-ray diffraction imaging (3D-CXDI) based on synchrotron radiation [75,80]. CXDI works in ambient conditions and with an easier sample preparation that does not require specific treatments like tinning. It is a lens-less imaging technique where the electron density distribution of an isolated object in real space is retrieved by an iterative algorithm that phases

an oversampled speckle pattern recorded in reciprocal space in the far field [75–77]. The technique provides the three-dimensional distribution of the electronic density on the basis of the local structure of the material (i.e., a combination of morphology and stoichiometry) with a resolution of a few tens of nanometers [78,81]. Here the electronic densities are given in absolute units ($e^-/\text{\AA}^3$) after normalization of the diffraction patterns to the incident intensity and beam size (see Materials and Methods). The voxel (volumetric picture element, i.e., the pixel in the 3D space) size is 17.8 nm.

3D-CXDI has been applied to image isolated fragments of TiO_2 layers deposited on a Si_3N_4 membrane (see Video S1 as Supplementary Material). Before the measurements, the sample was annealed at 500 °C in order to promote a lattice order in the anatase polymorphism without significantly upsetting the layer porosity [15,38,48]. Fragments of dimension in the range 2–5 μm were selected by optical inspection to meet the oversampling requirements (see Experimental Methods). Figure 2 shows a section (slice), the 3D image and the 3D electronic density distribution of a fragment of a pure TiO_2 scaffold. The reconstruction reveals a highly heterogeneous structure with pores having a large distribution in size, inherent to the gig-lox deposition method. With the voxel size of 17.8 nm, 3D-CXDI is well suited to image the meso-porosity both by slicing the fragment or by the 3D-reconstruction.

Additionally, we evaluated the average meso-porosity of the sponge within the fragments by computing the surface-to-volume ratio (SVR) of the reconstructed images using the Chimera [82] software (Figure 2b). The obtained value of 0.06 nm^{-1} corresponds to the SVR expected from a rods structure with rods having radius $\sim 33 \text{ nm}$ [48] according to the expression for a cylindrical shape:

$$\frac{S}{V} = \frac{2\pi rL}{\pi r^2L} = \frac{2}{r} = 0.06 \text{ nm}^{-1} \rightarrow r = 33 \text{ nm}. \quad (2)$$

The extracted radius accounts for the meso-structure of the material as described by the TEM cross-section images [48].

Micro-porosity cannot be directly resolved by 3D-CXDI; nevertheless, it has an indirect impact on the absolute value of the electronic density, being consequently lower than the anatase reference. A lower density of the matrix relates to the degree of porosity (see Figure 2a), according to Equation (1), modified as follows [83]:

$$P(\%V) = \left[1 - \left(\frac{\rho_{\text{matrix}}}{\rho_{\text{anatase}}}\right)\right] \times 100, \quad (3)$$

where ρ_{matrix} and ρ_{anatase} are the locally sampled electronic densities of the porous TiO_2 and anatase ($1.08 e^-/\text{\AA}^3$), respectively. The matrix component is extracted by the “Trainable Weka Segmentation” plugin in the Fiji software [84]. By creating a histogram of the matrix voxel values over all the reconstruction slices, the average electronic density can be determined. We found an average electronic density of the TiO_2 scaffold $\rho_{\text{matrix}} = 0.63 e^-/\text{\AA}^3$, indicating a degree of porosity (P(%)), $P(\%) \sim 42\%$, a value which is in agreement with the data in Figure 1a after auto-seeds formation, witnessing the sensitivity of 3D-CXDI to micro-porosity.

To disclose and support the relationship between micro- and meso-porosity [73,74], we complemented the CXDI analysis with EEP and scanning-TEM investigations.

3.2.2. EEP Analyses

EEP is used to quantitatively measure the layer porosity at the nano-scale and to gain insight on the pore size distribution, especially for the small pores. This technique measures the changes of the refractive index during adsorption and capillary condensation of a solvent (here isopropanol) into the pores of the material. The results are shown in Figure 2. The volume fraction of adsorbed isopropanol is deduced from the Bruggeman effective medium approximation (BEMA) which compares the refractive index of the empty film (void + TiO_2) with that of the film full of isopropanol (isopropanol + TiO_2) [79]. In this calculation, the fraction of TiO_2 remains fixed and the fraction of voids (accessible porosity) is considered to be equal to the fraction of isopropanol. The analysis was performed using a refractive index of 2.65 for the as-deposited sample, supposing a mixture of anatase and rutile in the local

ordering of the amorphous phase; for the samples annealed at 500 °C sample, being purely anatase [37], we used a refractive index of 2.53.

Based on what was previously found [48], cylindrical pores will be used for the calculation of pore size distribution (pore aspect ratio = 10). To a direct comparison, the TEM cross-section image in Figure 3a is additionally provided with details meso-/micro-pores [73,74] and on the internal nano-structuration of the TiO₂ columns (see Figure 1). Pore size distribution (in terms of their diameter) is given in adsorption and in desorption conditions. In adsorption, the average pore diameter is probed while in desorption the average diameter of the interconnection between pores is determined. In Figure 3b that the plot dV/dD gives the distribution of pore size diameter as a function of the number of pores [79]. Large pores will be less visible on this graph even if they can represent a large volume of the total porosity. Indeed, for a given contribution in term of volume, the number of large pores will be lower than the number of small pores.

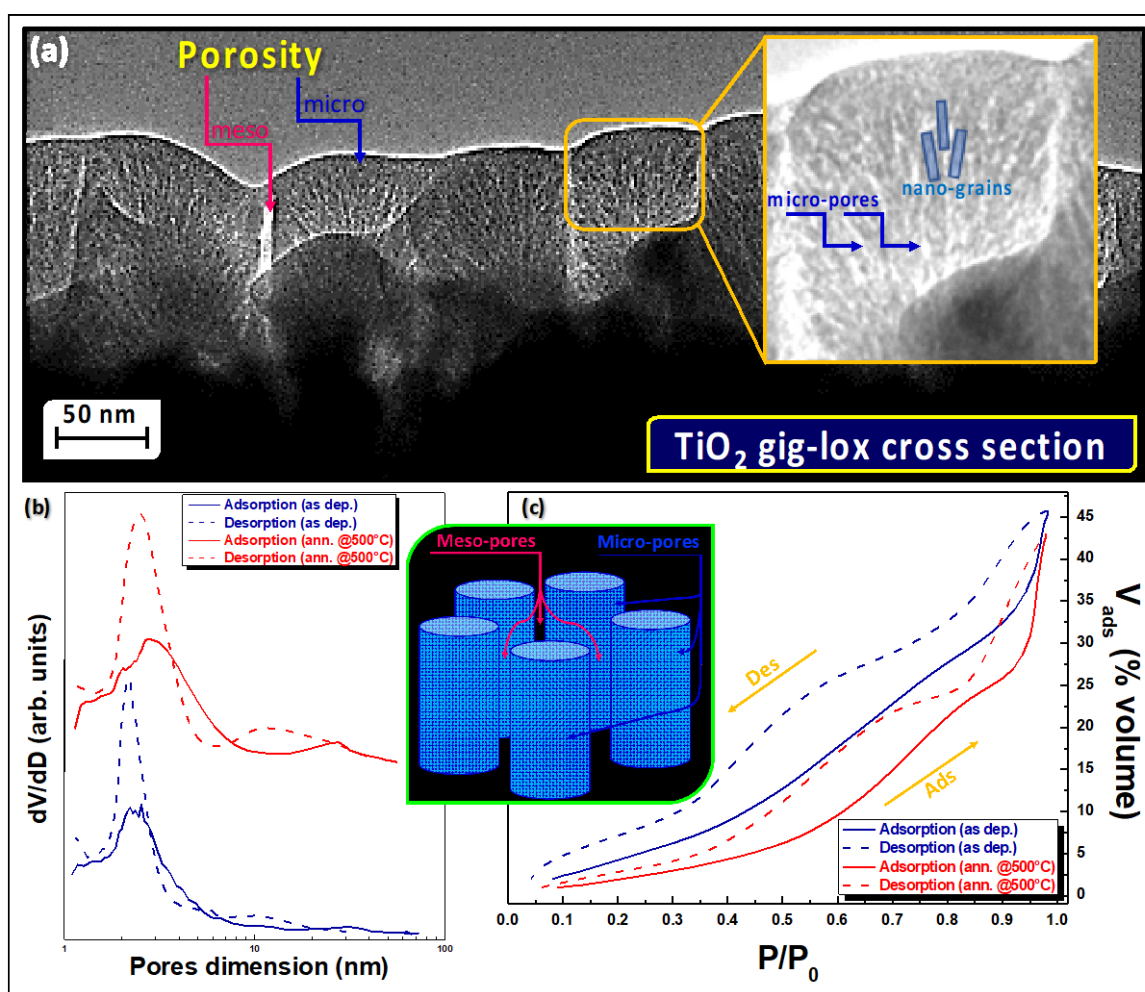


Figure 3. (a) TEM cross section of the gig-lox layer showing the material arrangement by nano-grains in a matrix of interconnected micro-pores (zoom in the yellow region). (b) Pore size distribution deduced from the Kelvin law for cylindrical interconnected pores for TiO₂ gig-lox in as-deposited and after annealing at 500 °C conditions. (c) Volume of adsorbed gas as a function of P/P_0 for TiO₂ gig-lox in as-deposited and after annealing at 500 °C conditions.

The pore size distribution in Figure 3b highlights some main points: (1) the bimodal distribution of the pores; (2) the persistence of small-size pores even after the thermal treatment at 500 °C; (3) a slight enlargement of the distribution after annealing and a small shift of the maximum rightwards that accounts for a slight increase of the average pore size (further discussed in the next paragraphs). Those

small changes are mainly related to the thermal contraction of TiO₂ occurring during crystallization to anatase (a further contribution of pore sintering is not excluded).

In order to get a good vision over the pore distribution in term of volumetric percentage, it is preferable to consider the plot of V_{ads} as a function of P/P_0 (where P_0 is the absolute pressure of the adsorbate) [79]. The total percentage of porosity slightly decrease after annealing at 500 °C. The bimodal distribution of the pores is visible by the changes in the slope around a partial pressure of 0.7 ($P/P_0 = 0.7$) corresponding to small pores and around a partial pressure of 0.9 ($P/P_0 = 0.9$) corresponding to large pipelines. Roughly half of the porosity (in volume) is accounted for by the large pores and half by the small pores. By comparison between the refractive index of the layers before and after isopropanol adsorption and the bulk refractive index of the material, we deduce that a part of the porosity is occluded (not probed by isopropanol). In particular, 20% of the empty volume is not accessible before annealing. After annealing, the fraction of occluded porosity diminishes to less than 10% of the material volume likely due to a contraction of the TiO₂ matrix with temperature.

Furthermore, those results demonstrate that the hierarchical porous network is well interconnected as smaller and larger pores (main large pipelines) are probed via diffusion and condensation of isopropanol. For further structural confirmation, see the inset in Figure 3a.

3.3. MAPbI₃ Loading

MAPbI₃ was deposited to enter the gig-lox structure via solution processing, as described in the methods section. The upper inset in Figure 4 shows the diffraction pattern of the synthesized perovskite with its typical tetragonal structure [44]. Fragments of the MAPbI₃/TiO₂ blend were prepared and analyzed by 3D-CXDI similarly as done for pure TiO₂ (see Figure 2). The advantage of using this approach for analyses resides in the lack of any special preparation procedure, as instead needed for TEM analyses; and this is extremely crucial when dealing with hybrid perovskites such as MAPbI₃ to avoid immediate degradation of the sample [85]. Representative reconstructions are shown in Figure 4. The upper row refers to a MAPbI₃/TiO₂ blend after deposition. The sections (see Figure 4a) locally reveal a largely compact morphology with an average volumetric electron density substantially higher than that of the empty TiO₂ scaffold. The compactness of the sample (see Figure 4b) and the raised density account for the perovskite having filled the mesopores of the scaffold during the solution processing. To see how MAPbI₃ entered the porous TiO₂ scaffold, we applied the Weka segmentation method to isolate the matrix and quantify the average electron density. This was $0.88 \text{ e}^-/\text{\AA}^3$, 40% larger than what found for the TiO₂ particles. The expected density for a pure MAPbI₃ sample is $1.05 \text{ e}^-/\text{\AA}^3$, while the TiO₂ scaffold has $\rho_{\text{matrix}} = 0.63 \text{ e}^-/\text{\AA}^3$. Figure 4c also reveals clusters at high electronic density ($>1.3 \text{ e}^-/\text{\AA}^3$), likely accounting for a local sporadic compositional change in the perovskite layer towards PbI₂ [42,44,45,48] (the electronic density of PbI₂ is $1.51 \text{ e}^-/\text{\AA}^3$).

The lower row of Figure 4e,f shows the effect of the full degradation of MAPbI₃ into PbI₂ (yellow sample) after prolonged exposure of the sample to air (see also the related XRD pattern in the inset). For this sample, the electronic density distribution of Figure 4f depicts a scenario of PbI₂ distributed all over the sample volume, with part of the iodide percolated inside vertical mesopores of the TiO₂ scaffold.

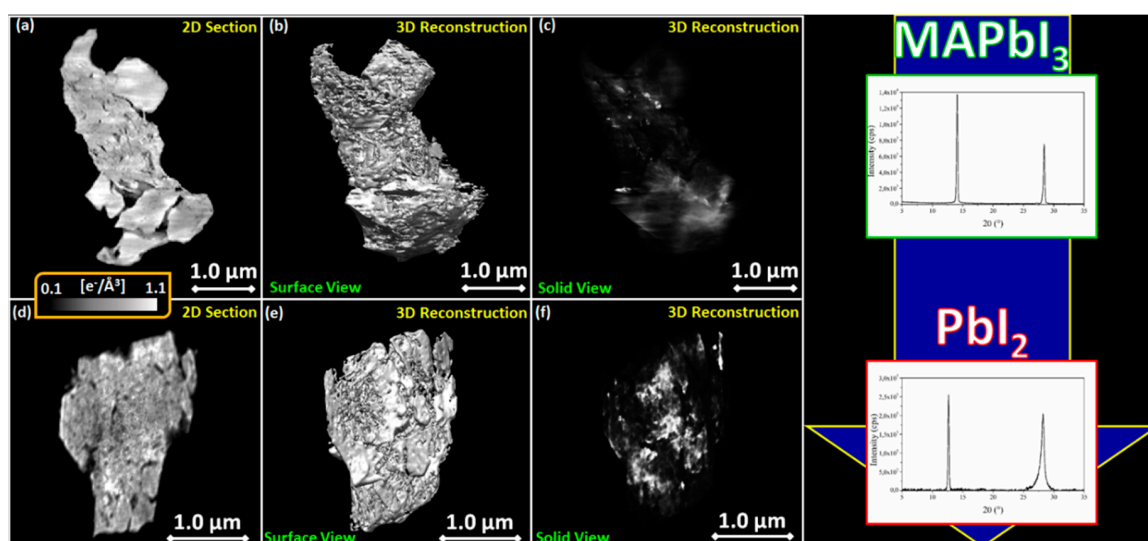


Figure 4. CXDI images of (a–c) a blend of TiO₂ and MAPbI₃; (d–f) a blend of TiO₂ and PbI₂. The brilliant zones in (c,f) correspond to material with high electronic density ($>$ anatase, TiO₂). As representative of the others, in (f) the brilliant rows (regions of density above $0.9\text{--}1\text{ e}^-/\text{\AA}^3$) of PbI₂ embedded into the matrix mark the infiltration path of MAPbI₃ into the vertical meso-pipelines. The color bar refers to all 2D sections.

Figure 5 plots the histograms of the matrix of the three investigated samples: the pure gig-lox scaffold; the scaffold infiltrated with perovskite (starting blend) and the blend after degradation. Through the distribution, a rationalization on the perovskite infiltration capability is drawn. The data additionally depict a scenario on how the perovskite modifies inside the TiO₂ scaffold as an effect of ageing in air. On this basis, the electronic density in the pure TiO₂ scaffold has a large distribution with mean value at $0.63\text{ e}^-/\text{\AA}^3$ and width (FWHM) $\sim 0.4\text{ e}^-/\text{\AA}^3$, which can be viewed as a combination of micro-porosity (the mean value) and meso-porosity (the width) [73,74]. The distribution intercepts the compact anatase density at the high-density tail. After blending with the perovskite, the histogram shifts rightwards since the loading increases the average electron density. At this stage, the percentage of free volume drops from $P \sim 42\%$ to $P \sim 18\%$. We point out that this last value could be overestimated with respect to the starting blend condition since even a small degradation of the perovskite in the fragment due to ambient exposure [44,45] would notably increase the fraction of the empty volume (a volume contraction by 54% occurs as a MAPbI₃ degrades to PbI₂). As soon as the phase conversion to PbI₂ is completed by prolonged exposure (several days), the histogram moves back leftwards. The minor extent of this shift depends on the interplay between the higher electronic density of the PbI₂ and the increase in porosity arising from the volume contraction during degradation, producing an average electron density slightly smaller ($0.80\text{ e}^-/\text{\AA}^3$). The Perovskite back-transition to PbI₂ can be easily identified inside the fragment in the 3D-reconstruction of CXDI data (solid view), and this especially traces the starting distribution of the host material through the mesopores (vertical brilliant zones in Figure 4f).

Resolving the perovskite distribution inside the micro-pores is beyond the resolution of the CXDI measurements. Therefore, scanning TEM (STEM) analyses were used to complement the information at the nano-scale. Following the approach adopted in the CXDI-based diagnostic for meso-pores, a marker was used to follow the infiltration path in the nano-gaps. A sample was, at this purpose, prepared by focused ion beam thinning procedure and analyzed by STEM in cross-section at a base pressure of $\sim 10^{-9}$ Torr. Under these adverse conditions the perovskite layer has a reduced lifetime [86] and even Pb nanoclusters can be formed [46]. We exploited the MAPbI₃ conversion into Pb-nanoclusters to trace the pristine perovskite distribution into the sponge. The method is especially effective to highlight micro-pores since the size of the Pb-clusters is comparable to the pore size. Deep and

capillary perovskite soaking was indeed testified by the spreading of those Pb-nanoclusters through the whole layer along rows that are made brilliant in STEM by the high mass of the lead atoms. Some representative images are shown in Figure 6.

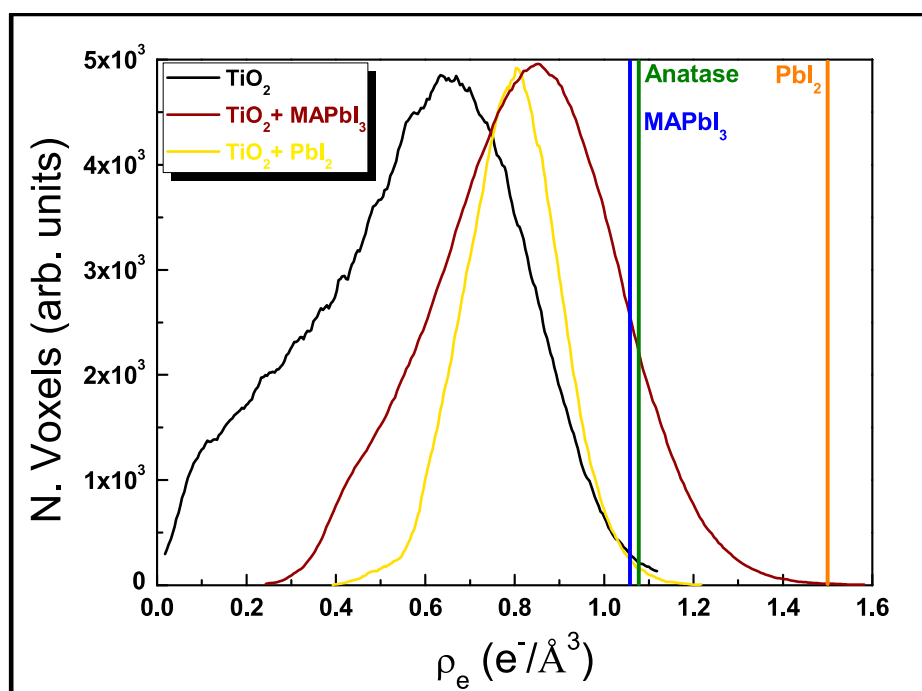


Figure 5. Electronic density distribution measured by CXDI in pure gig-lox TiO_2 , in the TiO_2 - MAPbI_3 blend and in the TiO_2 - PbI_2 blend.

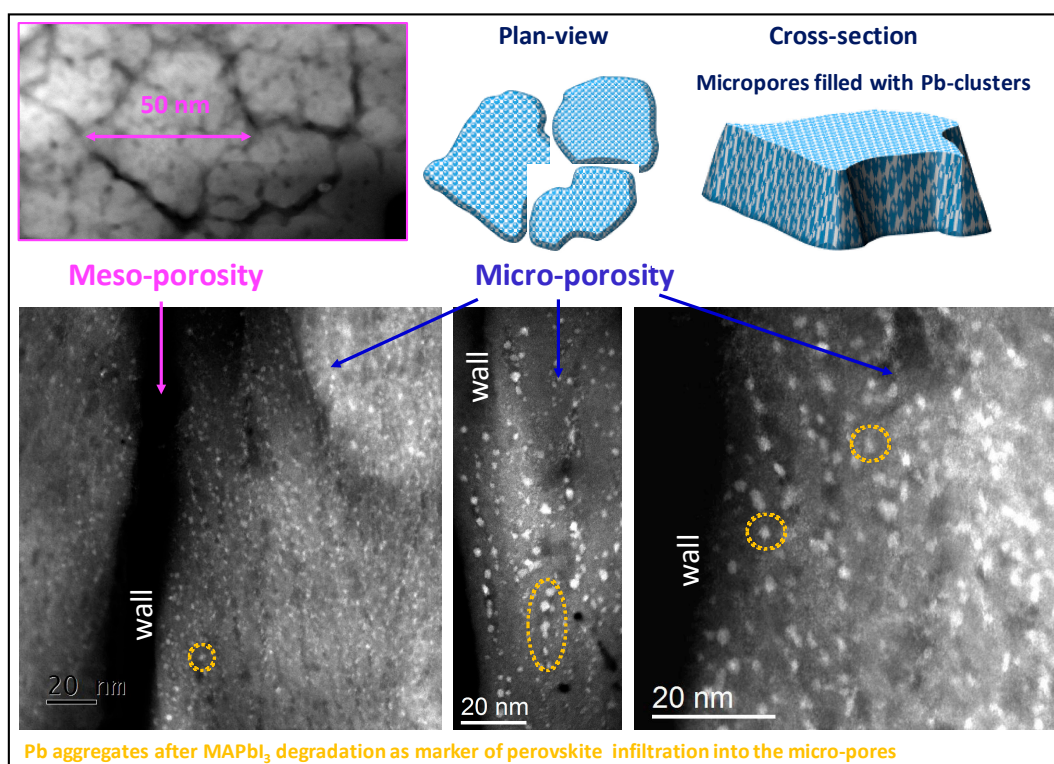


Figure 6. Scanning transmission electron microscopy images of the TiO_2 - MAPbI_3 blend after degradation of the perovskite to PbI_2 and Pb aggregation. Pb nanoclusters are used as markers to trace the initial distribution of the perovskite into the micro-pores (some of them are circled in yellow).

3.4. MAPbI₃/TiO₂ Blend Stability

One main concern on the blend to be applied is its durability under sun irradiation. This is firstly because the temperature of the blend is expected to increase with a possible impact on its stability. The maximum temperature during operation under the sun is expected to be in the range of 60–80 °C. In the experiment designed to test the thermal stability of the MAPbI₃–TiO₂ blend, the sample was kept under isothermal annealing in the range of 90–135 °C in controlled atmosphere, as schematically depicted in Figure 7. The range was chosen to apply a stress test to mimic prolonged operation conditions. As a testing procedure, the structural modification of the perovskite was traced by collecting its diffraction pattern during time at a fixed temperature, while the diffraction chamber was kept at 55 ± 5% HR (relative humidity), intentionally under the threshold to form hydrated perovskites [87,88]. A fresh sample was used for each temperature. During annealing and in a time frame proportional to the temperature used, all infiltrated materials were seen to progressively change their composition from MAPbI₃ to PbI₂. Consistently, the color of the sample changed from brown to yellow as shown in the upper panel of Figure 7. This was testified by the progressive consumption of the MAPbI₃ area of the main peak at 2θ = 14.00° ((002)/(110)) and the simultaneous increase of the PbI₂ peak at 2θ = 12.6° ((003) planes of the 9R hexagonal structure).

We measured the ((110)/(002)) MAPbI₃ peak area during time (Figure 7a) and converted this value into a mass variation according to [89] and applying the equation:

$$y = [\text{MAPbI}_3 \text{ \%}] = \left[\left(\frac{A_0}{A_i(t)} \right) \times 100 \right], \quad (4)$$

where A_0 is the area of the (002) peak at $t = 0$ and A_i is the corresponding area at $t = t_i$. The parameter can be used as a marker for the material degradation on the basis of some experimental observations, i.e., excluding a re-orientation of the original crystal lattice and with texturing maintained as in the starting condition. With this method, we find out that the degradation curves follow a decreasing trend. In Figure 7b we show the data recorded in air conditions, namely in the presence of moisture. For all the temperatures analyzed, the rate of the degradation is constant and thus the curves follow zero order kinetics. The kinetic constant k governing the process was extracted as:

$$y = [\text{MAPbI}_3 \text{ \%}] = [k(T) \times t]. \quad (5)$$

Used in an Arrhenius plot as

$$k(T) = k_0 e^{-\frac{E_a}{K_B T}}, \quad (6)$$

where K_B is the Boltzmann constant, the parameter can be applied to extract the activation energy of the degradation process. The value obtained for degradation reaction of the MAPbI₃ in air ambient is ~0.87 eV. This energy can be associated to a mechanism of degradation via volatilization of species from the lattice, being in the range of typical dissociation energies reported in the literature [41]. Although the value for perovskite degradation in the blend is lower by ~0.1 eV than that found in a flat layered material, the degradation times are roughly comparable (due to the non-negligible role of the pre-exponential factor) as commented in what follows. In the degradation process, MAI and/or HI, being both volatile species, are expected as by-products [90] mostly in the presence of water molecules, that have a catalytic action in activating their formation [42,91]. As a matter of fact, the identical experiment done in dry nitrogen is found to be governed, temperature by temperature, by lower kinetics constants with an associated activation energy of 0.99 eV.

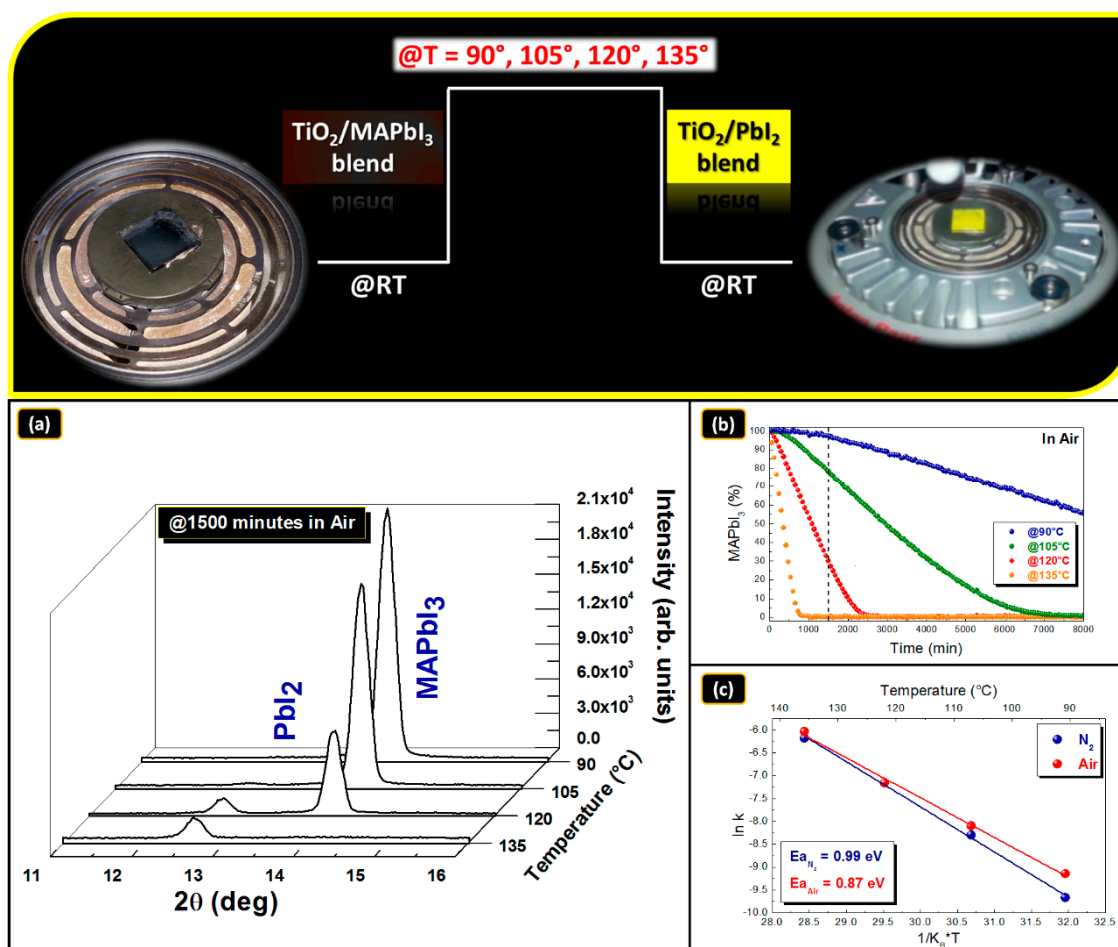


Figure 7. (a) XRD patterns collected after at 1500 min annealing in air at different temperatures; (b) kinetic analysis and fitting of the degradation curves of blend samples annealed at four different temperatures (90 °C, 105 °C, 120 °C and 135 °C) in air; (c) Arrhenius plot of the kinetic constant and activation energy extracted in air and dry N₂ environment. All data were collected in dark conditions.

In their summary, our findings not only shine light on the degradation mechanism of the perovskite in the blend, which is similar to what occurs in layers of perovskites, but additionally have a predictive role on what is expected in the operation range of temperatures under adverse (humid air) vs. inert (N₂) conditions. It must indeed be noticed that the two curves in Figure 7c tend to diverge at low temperatures, and this accounts for a better stability of the material under nitrogen conditions. We summarized the half-life times of the perovskite in Table 1:

Table 1. Half-life time of the perovskite in the blend under continuous operation at the indicated temperatures.

T (°C)	N ₂	Air
30	8854 days	1410 days
60	210 days	70 days
80	25 days	12 days

The table highlights the stabilization action of the overall blend via dry nitrogen and this suggests that the multiplication of interfaces with TiO₂, expected as instability sources, plays a minor role with respect to the environment. This demonstrates that our blend made of the gig-lox TiO₂ scaffold plus the infiltrated perovskite has a durability useful for application. Moreover, the half-life time measured at a working temperature of 60 °C under air conditions is comparable to that exhibited by a similar

perovskite layer deposited on flat TiO₂ as reported in our previous work [42]. This indeed implies that a blended architecture based on the gig-lox scaffold can be alternatively applied to standard layered architecture, with advantages likely offered by the extended surfaces available for charge extraction and collection.

4. Conclusions

To conclude, in exploring the early stages of the growth of the gig-lox TiO₂ sponge, auto-seeds are found to frame the bimodality of the generated pores. At first, a transient condition is established wherein the deposition rate is high and this corresponds to the maximum measured porosity. After that, moving towards a steady-state condition, hundred-nm auto-seeds are statistically generated and selected for further growth by the inclined ad-atoms and the shadowing effect. The resulting meso-grains contain the original nano-seeds and micro-porosity defined during the early stages of growth. In both steps, a bottom-up oxidation process is assured by a piloted oxygen path, independent from the Ar path and flow.

At the steady-state of the growth process, an overall porosity above 47% is established in the layer. Tomographic X-ray imaging (CXDI) acquired with synchrotron radiation on fragments of samples revealed a meso-porosity in the range ~10–100 nm that was subsequently exploited for perovskite loading. CXDI 3D-Imaging depicted a scenario of large perovskite infiltration along the meso-pores by mapping the electronic density distribution per unit volume into fragments of the blend, with pore filling estimated above 80% in volume. Although micro-pores are under the resolution of the technique, their accessibility is testified through complementary STEM analyses. MAPbI₃ conversion to PbI₂ or Pb was detected by CXDI and STEM with spatial distribution and resolution at the meso and micro scales, respectively, for the rationalization on the high capability of a gig-lox TiO₂ scaffold to form an intercalated blend with state-of-the-art hybrid photo-active materials.

The degradation of the perovskite in the blend, explored by a stress test experiment, follows a degradation path towards the formation of PbI₂ as solid by-product with the concomitant release of volatile species that need an activation energy sensitive to the environment used. The presence of humid air and nitrogen differently impacts on the value, with a delta of ~0.1 eV in favor of the inert environment that extends the half-life of the material to 7 months under continuous operation at 60 °C. The degradation process is indeed triggered by the environmental composition (e.g., humid air) rather than being related to the multiple interfaces established inside the blend.

Supplementary Materials: The following are available online at <http://www.mdpi.com/2079-4991/9/9/1300/s1>, Video S1: TiO₂ 3D-Reconstruction by CXDI.

Author Contributions: A.A. conceived the new deposition method and designed the experiments; together with A.L.M., she made coordination actions and supervision of the manuscript. S.S. wrote the manuscript, performed the deposition of all the materials discussed in the paper and dealt with the CXDI data analyses. XRR and XRD measurements were done by E.S. G.M. performed SE measurements accompanied by data modeling. D.G. and T.B. performed EEP analyses. C.B. performed TEM analyses. F.Z. performed CXDI analyses. F.N. and C.S. critically revised the manuscript and contributed to data interpretation.

Funding: The project was partially supported by the Italian project BEYOND NANO Upgrade (CUP G66J17000350007) and by the bilateral project founded by CNR (Italy) and JSPS (Japan) for partial support of the research on PSC (CUP B56C18001070005). CNR gratefully acknowledges the project PON entitled “Tecnologia per celle solari bifacciali ad alta Efficienza a 4 terminali per utility scale”, called BEST-4U, financed by the Italian Ministry MIUR (CUP B88D19000160005).

Acknowledgments: We acknowledge Yuriy Chushkin for providing the software for the data treatment of the CXDI data, Carla Cristina Polo for helping with the WEKA segmentation software and Karim Lhoste for the technical support during the beam time at the ESRF. We also thank Murielle Salome for providing the E-SEM apparatus at ESRF.

Conflicts of Interest: The authors declare no conflict of interest.

References

1. Fujishima, A.; Honda, K. Electrochemical Photolysis of Water at a Semiconductor Electrode. *Nature* **1972**, *238*, 37–38. [[CrossRef](#)] [[PubMed](#)]
2. Liu, H.; Joo, J.B.; Dahl, M.; Fu, L.; Zeng, Z.; Yin, Y. Crystallinity control of TiO₂ hollow shells through resin-protected calcination for enhanced photocatalytic activity. *Energy Environ. Sci.* **2015**, *8*, 286–296. [[CrossRef](#)]
3. Zhuang, H.F.; Lin, C.J.; Lai, Y.K.; Sun, L.; Li, J. Some critical structure factors of titanium oxide nanotube array in its photocatalytic activity. *Environ. Sci. Technol.* **2007**, *41*, 4735–4740. [[CrossRef](#)] [[PubMed](#)]
4. Alberti, A.; Bongiorno, C.; Pellegrino, G.; Sanzaro, S.; Smecca, E.; Condorelli, G.G.; Giuffrida, A.E.; Cicala, G.; Latteri, A.; Ognibene, G.; et al. Low temperature sputtered TiO₂ nano sheaths on electrospun PES fibers as high porosity photoactive material. *RSC Adv.* **2015**, *5*, 73444–73450. [[CrossRef](#)]
5. Ong, W.J.; Tan, L.L.; Chai, S.P.; Yong, S.T.; Mohamed, A.R. Facet-Dependent Photocatalytic Properties of TiO₂-Based Composites for Energy Conversion and Environmental Remediation. *Chemosuschem* **2014**, *7*, 690–719. [[CrossRef](#)] [[PubMed](#)]
6. Ong, W.J.; Tan, L.L.; Chai, S.P.; Yong, S.-T.; Mohamed, A.R. Self-assembly of nitrogen-doped TiO₂ with exposed {001} facets on a graphene scaffold as photo-active hybrid nanostructures for reduction of carbon dioxide to methane. *Nano Res.* **2014**, *7*, 1528–1547. [[CrossRef](#)]
7. Liu, N.; Li, K.; Li, X.; Chang, Y.; Feng, Y.; Sun, X.; Cheng, Y.; Wu, Z.; Zhang, H. Crystallographic Facet-Induced Toxicological Responses by Faceted Titanium Dioxide Nanocrystals. *RSC Nano* **2016**, *10*, 6062–6073. [[CrossRef](#)]
8. Zhai, P.; Hsieh, T.Y.; Yeh, C.Y.; Reddy, K.S.K.; Hu, C.C.; Su, J.H.; Wei, T.C.; Feng, S.P. Trifunctional TiO₂ Nanoparticles with Exposed {001} Facets as Additives in Cobalt-Based Porphyrin-Sensitized Solar Cells. *Adv. Funct. Mater.* **2015**, *25*, 6093–6100. [[CrossRef](#)]
9. Seger, B.; Pedersen, T.; Laursen, A.B.; Vesborg, P.C.K.; Hansen, O.; Chorkendorff, I. Using TiO₂ as a conductive protective layer for photocathodic H₂ evolution. *J. Am. Chem. Soc.* **2013**, *135*, 1057–1064. [[CrossRef](#)]
10. Kang, Q.; Cao, J.; Zhang, Y.; Liu, L.; Xu, H.; Ye, J. Reduced TiO₂ nanotube arrays for photoelectrochemical water splitting. *J. Mater. Chem. A* **2013**, *1*, 5766. [[CrossRef](#)]
11. Cho, I.S.; Choi, J.; Zhang, K.; Kim, S.J.; Jeong, M.J.; Cai, L.; Park, T.; Zheng, X.; Park, J.H. Highly Efficient Solar Water Splitting from Transferred TiO₂ Nanotube Arrays. *Nano Lett.* **2015**, *15*, 5709–5715. [[CrossRef](#)]
12. Ji, Y.; Zhang, M.; Cui, J.; Lin, K.-C.; Zheng, H.; Zhu, J.J.; Samia, A.C.S. Highly-ordered TiO₂ nanotube arrays with double-walled and bamboo-type structures in dye-sensitized solar cells. *Nano Energy* **2012**, *1*, 796–804. [[CrossRef](#)]
13. Roy, P.; Kim, D.; Lee, K.; Spiecker, E.; Schmuki, P. TiO₂ nanotubes and their application in dye-sensitized solar cells. *Nanoscale* **2010**, *2*, 45–59. [[CrossRef](#)]
14. Alberti, A.; Renna, L.; Sanzaro, S.; Smecca, E.; Mannino, G.; Bongiorno, C.; Galati, C.; Gervasi, L.; Santangelo, A.; La Magna, A. Innovative spongy TiO₂ layers for gas detection at low working temperature. *Sens. Actuators B Chem.* **2018**, *259*, 658–667. [[CrossRef](#)]
15. Smecca, E.; Sanzaro, S.; Grosso, D.; Bottein, T.; Mannino, G.; Condorelli, G.G.; La Magna, A.; Alberti, A. Nitrogen doped spongy TiO₂ layers for sensors application. *Mater. Sci. Semicond. Process.* **2019**, *98*, 44–48. [[CrossRef](#)]
16. Smecca, E.; Sanzaro, S.; Galati, C.; Renna, L.; Gervasi, L.; Santangelo, A.; Condorelli, G.G.; Grosso, D.; Bottein, T.; Mannino, G.; et al. Porous Gig-Lox TiO₂ Doped with N₂ at Room Temperature for P-Type Response to Ethanol. *Chemosensors* **2019**, *7*, 12. [[CrossRef](#)]
17. Li, H.; Chen, Z.; Tsang, C.K.; Li, Z.; Ran, X.; Lee, C.; Nie, B.; Zheng, L.; Hung, T.; Lu, J.; et al. Electrochemical doping of anatase TiO₂ in organic electrolytes for high-performance supercapacitors and photocatalysts. *J. Mater. Chem. A* **2014**, *2*, 229–236. [[CrossRef](#)]
18. Chen, B.; Hou, J.; Lu, K. Formation mechanism of TiO₂ nanotubes and their applications in photoelectrochemical water splitting and supercapacitors. *Langmuir* **2013**, *29*, 5911–5919. [[CrossRef](#)]
19. Lai, Y.; Lin, L.; Pan, F.; Huang, J.; Song, R.; Huang, Y.; Lin, C.; Fuchs, H.; Chi, L. Bioinspired patterning with extreme wettability contrast on TiO₂ nanotube array surface: A versatile platform for biomedical applications. *Small* **2013**, *9*, 2945–2953. [[CrossRef](#)]

20. Huaqiong, X.W.; Huaqiong, L.P.T.; Yuekun Lai, L.; Huang, J.; Tang, Y.; Yang, L.; Chen, Z.; Zhang, K. Multifunctional wettability patterns prepared by laser processing on superhydrophobic TiO₂ nanostructured surfaces. *J. Mater. Chem. B Mater. Biol. Med.* **2014**, *3*, 342–347.
21. Gao, H.; Sun, M.; Lin, C.; Wang, S. Electrochemical DNA Biosensor Based on Graphene and TiO₂ Nanorods Composite Film for the Detection of Transgenic Soybean Gene Sequence of MON89788. *Electroanalysis* **2012**, *24*, 2283–2290. [[CrossRef](#)]
22. Chen, J.S.; Tan, Y.L.; Li, C.M.; Cheah, Y.L.; Luan, D.; Madhavi, S.; Boey, F.Y.C.; Archer, L.A.; Lou, X.W. Constructing hierarchical spheres from large ultrathin anatase TiO₂ nanosheets with nearly 100% exposed (001) facets for fast reversible lithium storage. *J. Am. Chem. Soc.* **2010**, *132*, 6124–6130. [[CrossRef](#)] [[PubMed](#)]
23. Wang, K.; Wei, M.; Morris, M.A.; Zhou, H.; Holmes, J.D. Mesoporous Titania Nanotubes: Their Preparation and Application as Electrode Materials for Rechargeable Lithium Batteries. *Adv. Mater.* **2007**, *19*, 3016–3020. [[CrossRef](#)]
24. Guo, W.; Xue, X.; Wang, S.; Lin, C.; Wang, Z.L. An integrated power pack of dye-sensitized solar cell and Li battery based on double-sided TiO₂ nanotube arrays. *Nano Lett.* **2012**, *12*, 2520–2523. [[CrossRef](#)] [[PubMed](#)]
25. De Angelis, F.; Kamat, P.A. A Conversation with Michael Grätzel. *RSC Energy Lett.* **2017**, *2*, 1674–1676. [[CrossRef](#)]
26. O'Regan, B.; Grätzel, M. A low-cost, high-efficiency solar cell based on dye-sensitized colloidal TiO₂ films. *Nature* **1991**, *353*, 737–740. [[CrossRef](#)]
27. Grätzel, M. Solar energy conversion by dye-sensitized photovoltaic cells. *Inorg. Chem.* **2005**, *44*, 6841–6851. [[CrossRef](#)] [[PubMed](#)]
28. Miyasaka, T. Perovskite Photovoltaics: Rare Functions of Organo Lead Halide in Solar Cells and Optoelectronic Devices. *Chem. Lett.* **2015**, *44*, 720–729. [[CrossRef](#)]
29. Idota, Y.; Kubota, T.; Matsufuji, A.; Maekawa, Y.; Miyasaka, T. Tin-based amorphous oxide: A high-capacity lithium-ion-storage material. *Science* **1997**, *276*, 1395–1397. [[CrossRef](#)]
30. Kogo, A.; Iwasaki, S.; Ikegami, M.; Miyasaka, T. An Ultrathin Sputtered TiO₂ Compact Layer for Mesoporous Brookite-based Plastic CH₃NH₃PbI_{3-x}Cl_x Solar Cells. *Chem. Lett.* **2017**, *46*, 530–532. [[CrossRef](#)]
31. Sulaeman, U.; Zuhairi Abdullah, A. The way forward for the modification of dye-sensitized solar cell towards better power conversion efficiency. *Renew. Sustain. Energy Rev.* **2017**, *74*, 438–452. [[CrossRef](#)]
32. Ge, M.; Cao, C.; Huang, J.; Li, S.; Chen, Z.; Zhang, K.Q.; Al-deyab, S.S.; Lai, Y. A Review of One-dimensional TiO₂ Nanostructured Materials for Environmental and Energy Applications. *J. Mater. Chem. A* **2016**, *4*, 6772–6801. [[CrossRef](#)]
33. Alberti, A.; De Marco, L.; Pellegrino, G.; Condorelli, G.G.; Giannuzzi, R.; Scarfiello, R.; Manca, M.; Spinella, C.; Gigli, G.; La Magna, A. Combined strategy to realize efficient photoelectrodes for low temperature fabrication of dye solar cells. *RSC Appl. Mater. Interfaces* **2014**, *6*, 6425–6433. [[CrossRef](#)] [[PubMed](#)]
34. Alberti, A.; Pellegrino, G.; Condorelli, G.G.; Bongiorno, C.; Morita, S.; La Magna, A.; Miyasaka, T. Efficiency enhancement in ZnO:Al-based dye-sensitized solar cells structured with sputtered TiO₂ blocking layers. *J. Phys. Chem. C* **2014**, *118*, 6576–6585. [[CrossRef](#)]
35. Pellegrino, G.; Condorelli, G.G.; Privitera, V.; Cafra, B.; Di Marco, S.; Alberti, A. Dye-Sensitizing of Self-Nanostructured Ti:(Zn)O₂/AZO Transparent Electrodes by Self-Assembly of 5,10,15,20-Tetrakis(4-carboxyphenyl)porphyrin. *J. Phys. Chem. C* **2011**, *115*, 7760–7767. [[CrossRef](#)]
36. Pellegrino, G.; Condorelli, G.G.; De Rossi, F.; Brown, T.M.; Giovenale, F.; Bongiorno, C.; Alberti, A. Thermally induced structural modifications of nano-sized anatase films and the effects on the dye-TiO₂ surface interactions. *Appl. Surf. Sci.* **2014**, *296*, 69–78. [[CrossRef](#)]
37. Sanzaro, S.; La Magna, A.; Smecca, E.; Mannino, G.; Pellegrino, G.; Fazio, E.; Neri, F.; Alberti, A. Controlled Al³⁺ Incorporation in the ZnO Lattice at 188 °C by Soft Reactive Co-Sputtering for Transparent Conductive Oxides. *Energies* **2016**, *9*, 433. [[CrossRef](#)]
38. Alberti, A.; Bongiorno, C.; Pellegrino, G. Anatase/Rutile nucleation and growth on (0002) and (11–20) oriented ZnO:Al/glass substrates at 150 °C. *Thin Solid Film.* **2014**, *555*, 3–8. [[CrossRef](#)]
39. Colella, S.; Mosconi, E.; Pellegrino, G.; Alberti, A.; Guerra, V.L.P.; Masi, S.; Listorti, A.; Rizzo, A.; Condorelli, G.G.; De Angelis, F.; et al. Elusive presence of chloride in mixed halide perovskite solar cells. *J. Phys. Chem. Lett.* **2014**, *5*, 3532–3538. [[CrossRef](#)]

40. Pellegrino, G.; Colella, S.; Deretzis, I.; Condorelli, G.G.; Smecca, E.; Gigli, G.; La Magna, A.; Alberti, A. Texture of MAPbI₃ Layers assisted by Chloride on Flat TiO₂ Substrates. *J. Phys. Chem. C* **2015**, *119*, 19808–19816. [[CrossRef](#)]
41. Deretzis, I.; Alberti, A.; Pellegrino, G.; Smecca, E.; Giannazzo, F.; Sakai, N.; Miyasaka, T.; La Magna, A. Atomistic origins of CH₃NH₃PbI₃ degradation to PbI₂ in vacuum. *Appl. Phys. Lett.* **2015**, *106*, 131904–131917. [[CrossRef](#)]
42. Smecca, E.; Numata, Y.; Deretzis, I.; Pellegrino, G.; Boninelli, S.; Miyasaka, T.; La Magna, A.; Alberti, A. Stability of solution-processed MAPbI₃ and FAPbI₃ layers. *Phys. Chem. Chem. Phys.* **2016**, *18*, 13413–13422. [[CrossRef](#)] [[PubMed](#)]
43. Deretzis, I.; Di Mauro, B.N.; Alberti, A.; Pellegrino, G.; Smecca, E.; La Magna, A. Spontaneous bidirectional ordering of CH₃NH₃⁺ in lead iodide perovskites at room temperature: The origins of the tetragonal phase. *Sci. Rep.* **2016**, *6*, 24443–24452. [[CrossRef](#)] [[PubMed](#)]
44. Alberti, A.; Deretzis, I.; Mannino, G.; Smecca, E.; Sanzaro, S.; Numata, Y.; Miyasaka, T.; La Magna, A. Revealing a Discontinuity in the Degradation Behavior of CH₃NH₃PbI₃ during Thermal Operation. *J. Phys. Chem. C* **2017**, *121*, 13577–13585. [[CrossRef](#)]
45. Mannino, G.; Alberti, A.; Deretzis, I.; Smecca, E.; Sanzaro, S.; Numata, Y.; Miyasaka, T.; La Magna, A. First Evidence of CH₃NH₃PbI₃ Optical Constants Improvement in a N₂ Environment in the Range 40–80 °C. *J. Phys. Chem. C* **2017**, *121*, 7703–7710. [[CrossRef](#)]
46. Alberti, A.; Mannino, G.; Deretzis, I.; Smecca, E.; Sanzaro, S.; La Magna, A.; Numata, Y.; Miyasaka, T. Structural and Optical Behaviour of MAPbI₃ Layers in Nitrogen and Humid Air. In Proceedings of the 2018 IEEE 4th International Forum on Research and Technology for Society and Industry (RTSI), Palermo, Italy, 10–13 September 2018.
47. Alberti, A.; Deretzis, I.; Pellegrino, G.; Bongiorno, C.; Smecca, E.; Mannino, G.; Giannazzo, F.; Condorelli, G.G.; Sakai, N.; Miyasaka, T.; et al. Similar Structural Dynamics for the Degradation of CH₃NH₃PbI₃ in Air and in Vacuum. *Chemphyschem* **2015**, *16*, 3064–3071. [[CrossRef](#)] [[PubMed](#)]
48. Sanzaro, S.; Smecca, E.; Mannino, G.; Bongiorno, C.; Pellegrino, G.; Neri, F.; Malandrino, G.; Catalano, M.R.; Condorelli, G.G.; Iacobellis, R.; et al. Multi-Scale-Porosity TiO₂ scaffolds grown by innovative sputtering methods for high throughput hybrid photovoltaics. *Sci. Rep.* **2016**, *6*, 39509–39524. [[CrossRef](#)]
49. Sanzaro, S.; Fazio, E.; Neri, F.; Smecca, E.; Bongiorno, C.; Mannino, G.; Puglisi, R.A.; La Magna, A.; Alberti, A. Pervasive infiltration and multi-branch chemisorption of N-719 molecules into newly designed spongy TiO₂ layers deposited by gig-lox sputtering processes. *J. Mater. Chem. A* **2017**, *5*, 25529–25538. [[CrossRef](#)]
50. Palazon, F.; Pérez-del-Rey, D.; Marras, S.; Prato, M.; Sessolo, M.; Bolink, H.J.; Manna, L. Coating Evaporated MAPI Thin Films with Organic Molecules: Improved Stability at High Temperature and Implementation in High-Efficiency Solar Cells. *ACS Energy Lett.* **2018**, *3*, 835–839. [[CrossRef](#)]
51. Alberti, A.; Bongiorno, C.; Smecca, E.; Deretzis, I.; La Magna, A.; Spinella, C. Pb clustering and PbI₂ nanofragmentation during methylammonium lead iodide perovskite degradation. *Nat. Commun.* **2019**, *10*, 2196. [[CrossRef](#)]
52. Alberti, A.; Deretzis, I.; Mannino, G.; Smecca, E.; Giannazzo, F.; Listorti, A.; Colella, S.; Masi, S.; La Magna, A. Nitrogen soaking promotes lattice recovery in polycrystalline hybrid perovskites. *Adv. Energy Mater.* **2019**, *9*, 1803450. [[CrossRef](#)]
53. Alberti, A.; Smecca, E.; Sanzaro, S.; Mannino, G.; Deretzis, I.; La Magna, A. Hybrid perovskites for photovoltaics: Story, challenges and opportunities. *La Riv. Nuovo Cimento* **2019**, *42*, 301.
54. Cao, Y.; Saygili, Y.; Ummadisingu, A.; Teuscher, J.; Luo, J.; Pellet, N.; Giordano, F.; Zakeeruddin, S.M.; Moser, J.-E.; Freitag, M.; et al. 11% efficiency solid-state dye-sensitized solar cells with copper(II/I) hole transport materials. *Nat. Commun.* **2017**, *8*, 15390–15404. [[CrossRef](#)] [[PubMed](#)]
55. Lin, J.; Heo, Y.-U.; Nattestad, A.; Sun, Z.; Wang, L.; Kim, J.H.; Dou, S.X. 3D Hierarchical Rutile TiO₂ and Metal-free Organic Sensitizer Producing Dye-sensitized Solar Cells 8.6% Conversion Efficiency. *Sci. Rep.* **2015**, *4*, 5769. [[CrossRef](#)] [[PubMed](#)]
56. Lin, J.; Zhao, L.; Heo, Y.U.; Wang, L.; Bijarbooneh, F.H.; Mozer, A.J.; Nattestad, A.; Yamauchi, Y.; Dou, S.X.; Kim, J.H. Mesoporous anatase single crystals for efficient Co^(2+/3+)-based dye-sensitized solar cells. *Nano Energy* **2015**, *11*, 557–567. [[CrossRef](#)]

57. Lin, J.; Heo, Y.-U.; Nattestad, A.; Shahabuddin, M.; Yamauchi, Y.; Kim, J.H. N71- and D149-sensitized 3D hierarchical rutile TiO₂ solar cells—A comparative study. *Phys. Chem. Chem. Phys.* **2015**, *17*, 7208–7213. [[CrossRef](#)] [[PubMed](#)]
58. Thornton, J.A. The microstructure of sputter-deposited coatings. *J. Vac. Sci. Technol. A Vac. Surf. Film.* **1986**, *4*, 3059–3065. [[CrossRef](#)]
59. Movchan, B.A.; Demchishin, A.V. Structure and Properties of Thick Condensates of Nickel, Titanium, Tungsten, Aluminum Oxides and Zirconium Dioxide in Vacuum. *Fiz. Metal. Metalloved.* **1969**, *28*, 83–90.
60. Kang, S.H.; Kang, M.-S.; Kim, H.-S.; Kim, J.-Y.; Chung, Y.-H.; Smyrl, W.H.; Sung, Y.-E. Columnar rutile TiO₂ based dye-sensitized solar cells by radio-frequency magnetron sputtering. *J. Power Sources* **2008**, *184*, 331–335. [[CrossRef](#)]
61. Gómez, M.M.; Lu, J.; Olsson, E.; Hagfeldt, A.; Granqvist, C. High efficiency dye-sensitized nanocrystalline solar cells based on sputter deposited Ti oxide films. *Sol. Energy Mater. Sol. Cells* **2000**, *64*, 385–392. [[CrossRef](#)]
62. González-García, L.; González-Valls, I.; Lira-Cantu, M.; Barranco, A.; González-Elipe, A.R. Aligned TiO₂ nanocolumnar layers prepared by PVD-GLAD for transparent dye sensitized solar cells. *Energy Environ. Sci.* **2011**, *4*, 3426–3435. [[CrossRef](#)]
63. Li, Z.; Teng, Y.; Xing, L.; Zhang, N.; Zhang, Z. Enhancement of the photocatalytic property of TiO₂ columnar nanostructured films by changing deposition angle. *Mater. Res. Bull.* **2014**, *50*, 68–72. [[CrossRef](#)]
64. Motemani, Y.; Greulich, C.; Khare, C.; Lopian, M.; Buenconsejo, P.J.S.; Schildhauer, T.A.; Ludwig, A.; Köller, M. Adherence of human mesenchymal stem cells on Ti and TiO₂ nano-columnar surfaces fabricated by glancing angle sputter deposition. *Appl. Surf. Sci.* **2014**, *292*, 626–631. [[CrossRef](#)]
65. Pihosh, Y.; Turkevych, I.; Ye, J.; Goto, M.; Kasahara, A.; Kondo, M.; Tosa, M. Photocatalytic Properties of TiO₂ Nanostructures Fabricated by Means of Glancing Angle Deposition and Anodization. *J. Electrochem. Soc.* **2009**, *156*, K160–K165. [[CrossRef](#)]
66. Sanchez-Sobrado, O.; Mendes, M.J.; Haque, S.; Mateus, T.; Araujo, A.; Aguas, H.; Fortunato, E.; Martins, R. Colloidal-lithographed TiO₂ photonic nanostructures for solar cell light trapping. *J. Mater. Chem. C* **2017**, *5*, 6852–6861. [[CrossRef](#)]
67. Nunes, D.; Pimentel, A.; Santos, L.; Barquinha, P.; Fortunato, E.; Martins, R. Photocatalytic TiO₂ Nanorod Spheres and Arrays Compatible with Flexible Applications. *Catalysts* **2017**, *7*, 60. [[CrossRef](#)]
68. Smecca, E.; Sanzaro, S.; Bongiorno, C.; Giannazzo, F.; Mannino, G.; La Magna, A.; Liu, M.; Vivo, P.; Listorti, A.; Calabrò, E.; et al. Nano-structured TiO₂ grown by low-temperature reactive sputtering for planar perovskite solar cells. *RSC Appl. Energy Mater.* **2019**, in press.
69. Iza, D.C.; Muñoz-Rojas, D.; Musselman, K.P.; Weickert, J.; Jakowetz, A.C.; Sun, H.; Ren, R.L.Z.; Hoye, J.H.; Lee, X.; Wang, H.; et al. Nanostructured conformal hybrid solar cells: A promising architecture towards complete charge collection and light absorption. *Nanoscale Res. Lett.* **2013**, *8*, 359. [[CrossRef](#)]
70. Biswas, S.; Jiménez, C.; Khan, A.; Forissier, S.; Kar, A.K.; Muñoz-Rojas, D.; Deschamps, J.-L. Structural study of TiO₂ hierarchical microflowers grown by aerosol-assisted MOCVD. *Crystengcomm* **2014**, *19*, 1535–1544. [[CrossRef](#)]
71. Zhou, Q.; Li, Z.; Ni, J.; Zhang, Z. A Simple Model to Describe the Rule of Glancing Angle Deposition. *Mater. Trans.* **2011**, *52*, 469–473. [[CrossRef](#)]
72. Chen, S.; Li, Z.; Zhang, Z. Anisotropic Ti_xSn_{1-x}O₂ nanostructures prepared by magnetron sputter deposition. *Nanoscale Res. Lett.* **2011**, *6*, 326–330. [[CrossRef](#)] [[PubMed](#)]
73. Sing, K.S.W.; Everett, D.H.; Haul, R.A.W.; Moscou, L.; Pierotti, R.A.; Rouquérol, J.; Siemieniewska, T. Reporting physisorption data for gas/solid systems with special reference to the determination of surface area and porosity. *Pure Appl. Chem.* **1985**, *57*, 603–619. [[CrossRef](#)]
74. Following on Website: ISO/TS 80004-1:2010 Nanotechnologies-Vocabulary-Part 1: Core Terms. Available online: <https://www.iso.org/standard/51240.html> (accessed on 11 September 2019).
75. Miao, J.; Charalambous, P.; Kirz, J.; Sayre, D. Extending the methodology of X-ray crystallography to allow imaging of micrometre-sized non-crystalline specimens. *Nature* **1999**, *400*, 342–344. [[CrossRef](#)]
76. Sayre, D.; Chapman, H.N. X-ray microscopy. *Acta Crystallogr. Sect. A Found. Adv.* **1995**, *51*, 237–252. [[CrossRef](#)] [[PubMed](#)]
77. Sayre, D.; Chapman, H.N.; Miao, J. On the Extendibility of X-ray Crystallography to Noncrystals. *Acta Crystallogr. Sect. A Found. Crystallogr.* **1998**, *54*, 232–239. [[CrossRef](#)]

78. Chushkin, Y.; Zontone, F.; Lima, E.; De Caro, L.; Guardia, P.; Manna, L.; Giannini, C. Three-dimensional coherent diffractive imaging on non-periodic specimens at the ESRF beamline ID10. *J. Synchrotron Radiat.* **2014**, *21*, 594–599. [[CrossRef](#)] [[PubMed](#)]
79. Boissiere, C.; Grosso, D.; Lepoutre, S.; Nicole, L.; Bruneau, A.B.; Sanchez, C. Porosity and mechanical properties of mesoporous thin films assessed by environmental ellipsometric porosimetry. *Langmuir* **2005**, *21*, 12362–12371. [[CrossRef](#)]
80. Chapman, H.N.; Barty, A.; Marchesini, S.; Noy, A.; Hau-Riege, S.P. High-resolution ab initio three-dimensional X-ray diffraction microscopy. *J. Opt. Soc. Am. A* **2006**, *23*, 1179–1200. [[CrossRef](#)]
81. Skjønfsjell, E.T.B.; Chushkin, Y.; Zontone, F.; Patil, N.; Gibaud, A.; Breiby, D.W. Wavefront metrology for coherent hard X-rays by scanning a microsphere. *Opt. Express* **2016**, *24*, 10710–10722. [[CrossRef](#)]
82. Pettersen, E.F.; Goddard, T.D.; Huang, C.C.; Couch, G.S.; Greenblatt, D.M.; Meng, E.C.; Ferrin, T.E. UCSF Chimera—A visualization system for exploratory research and analysis. *J. Comput. Chem.* **2004**, *25*, 1605–1612. [[CrossRef](#)]
83. De Jong, E.M.L.D.; Mannino, G.; Alberti, A.; Ruggeri, R.; Italia, M.; Zontone, F.; Chushkin, Y.; Pennisi, A.R.; Gregorkiewicz, T.; Faraci, G. Strong infrared photoluminescence in highly porous layers of large faceted Si crystalline nanoparticles. *Sci. Rep.* **2016**, *6*, 25664. [[CrossRef](#)] [[PubMed](#)]
84. Schindelin, J.; Arganda-Carreras, I.; Frise, E.; Kaynig, V.; Longair, M.; Pietzsch, T.; Preibisch, S.; Rueden, C.; Saalfeld, S.; Schmid, B.; et al. Fiji: An open-source platform for biological-image analysis. *Nat. Methods* **2012**, *9*, 676–682. [[CrossRef](#)] [[PubMed](#)]
85. Deretzis, I.; Smecca, E.; Mannino, G.; La Magna, A.; Miyasaka, T.; Alberti, A. Stability and Degradation in Hybrid Perovskites: Is the Glass Half-Empty or Half-Full? *J. Phys. Chem. Lett.* **2018**, *9*, 3000–3007. [[CrossRef](#)] [[PubMed](#)]
86. Rothmann, M.U.; Li, W.; Zhu, Y.; Bach, U.; Spiccia, L.; Etheridge, J.; Cheng, Y.B. Direct observation of intrinsic twin domains in tetragonal $\text{CH}_3\text{NH}_3\text{PbI}_3$. *Nat. Commun.* **2017**, *8*, 14547. [[CrossRef](#)] [[PubMed](#)]
87. Leguy, A.M.A.; Hu, Y.; Campoy-Quiles, M.; Alonso, M.I.; Weber, O.J.; Azarhoosh, P.; Van Schilfgaarde, M.; Weller, M.T.; Bein, T.; Nelson, J.; et al. Reversible hydration of $\text{CH}_3\text{NH}_3\text{PbI}_3$ in films, single crystals, and solar cells. *Chem. Mater.* **2015**, *27*, 3397–3407. [[CrossRef](#)]
88. Yang, J.; Siempelkamp, B.D.; Liu, D.; Kelly, T.L. Investigation of $\text{CH}_3\text{NH}_3\text{PbI}_3$ degradation rates and mechanisms in controlled humidity environments using in situ techniques. *RSC Nano* **2015**, *9*, 1955–1963. [[CrossRef](#)] [[PubMed](#)]
89. Moore, D.T.; Sai, H.; Tan, K.W.; Smilgies, D.M.; Zhang, W.; Snaith, H.J.; Wiesner, U.; Estroff, L.A. Crystallization kinetics of organic-inorganic trihalide perovskites and the role of the lead anion in crystal growth. *J. Am. Chem. Soc.* **2015**, *137*, 2350–2358. [[CrossRef](#)] [[PubMed](#)]
90. Ciccioli, A.; Latini, A. Thermodynamics and the Intrinsic Stability of Lead Halide Perovskites $\text{CH}_3\text{NH}_3\text{PbX}_3$. *J. Phys. Chem. Lett.* **2018**, *9*, 3756–3765. [[CrossRef](#)] [[PubMed](#)]
91. Frost, J.M.; Butler, K.T.; Brivio, F.; Hendon, C.H.; Van Schilfgaarde, M.; Walsh, A. Atomistic origins of high-performance in hybrid halide perovskite solar cells. *Nano Lett.* **2014**, *14*, 2584–2590. [[CrossRef](#)]

